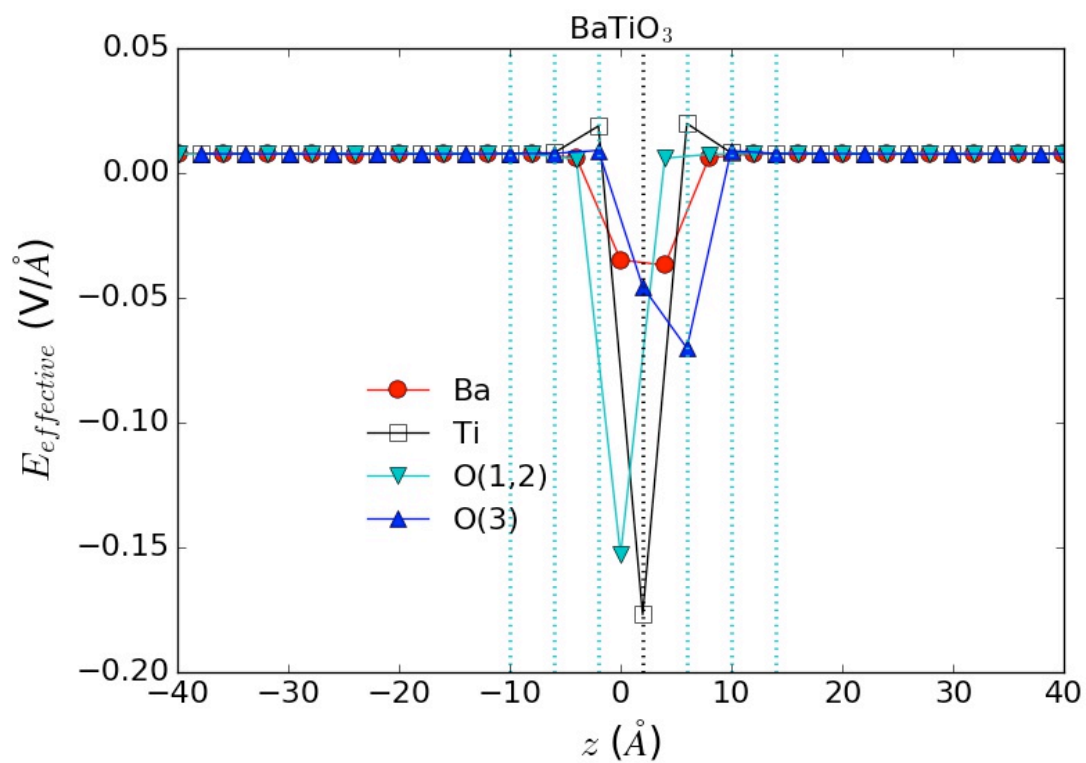


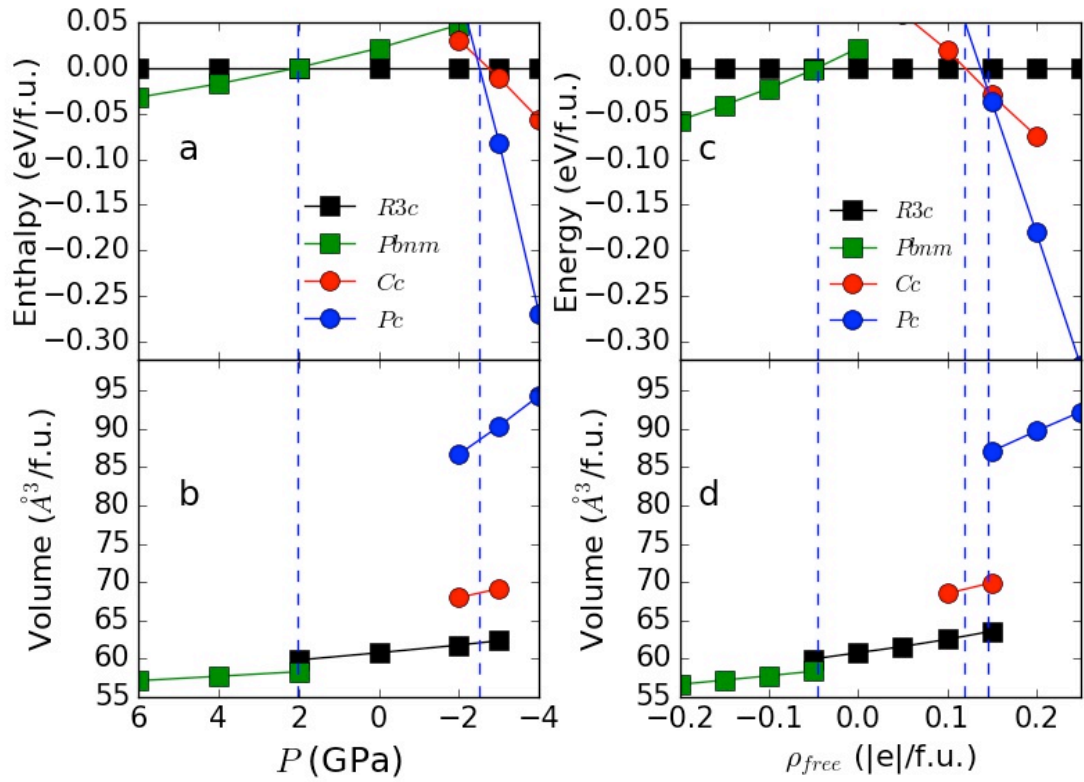
Supplemental Materials for

“Meta-screening and permanence of polar distortions in metallized ferroelectrics”,

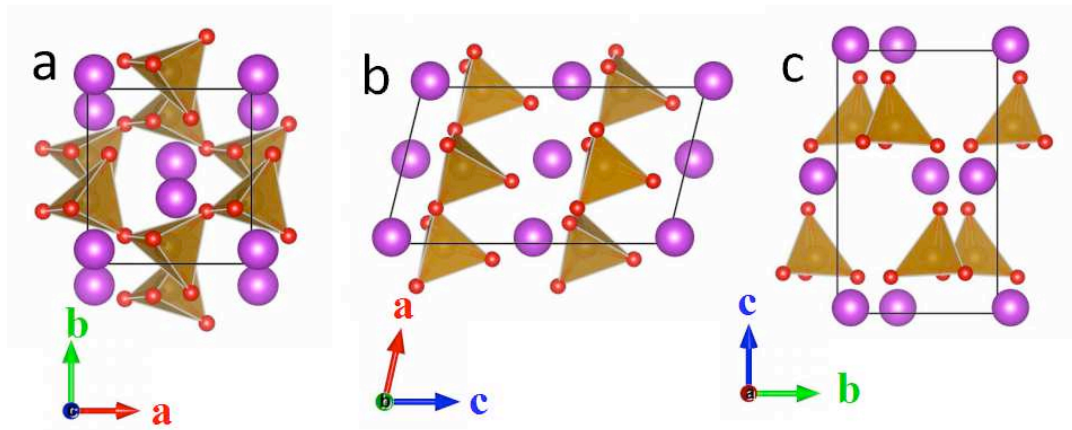
by Hong Jian Zhao, Alessio Filippetti, Carlos Escorihuela-Sayalero, Pietro Delugas,
Enric Canadell, L. Bellaiche, Vincenzo Fiorentini and Jorge Íñiguez.



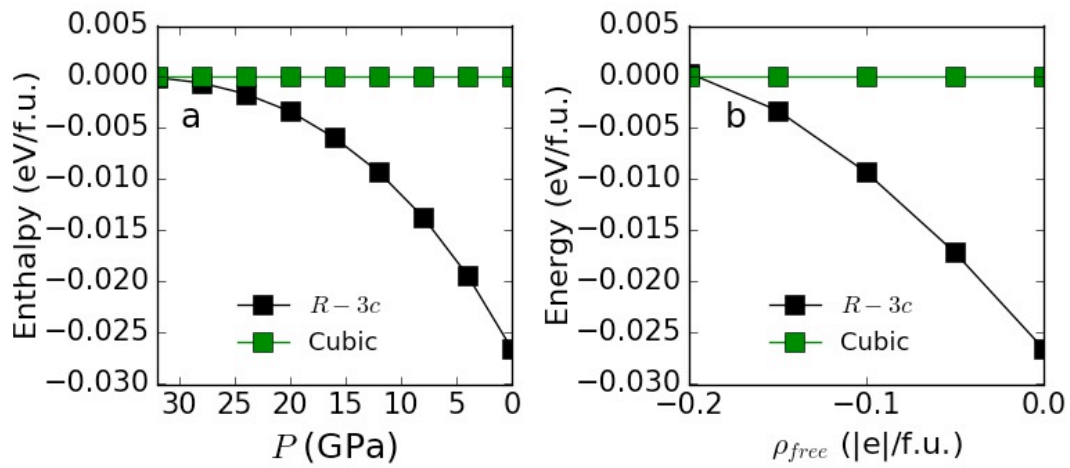
Supplementary Figure 1: Effective electric field [calculated by Supplementary Eq. (1)] acting on Ba, Ti, O(1), O(2) and O(3) atoms in BaTiO₃.



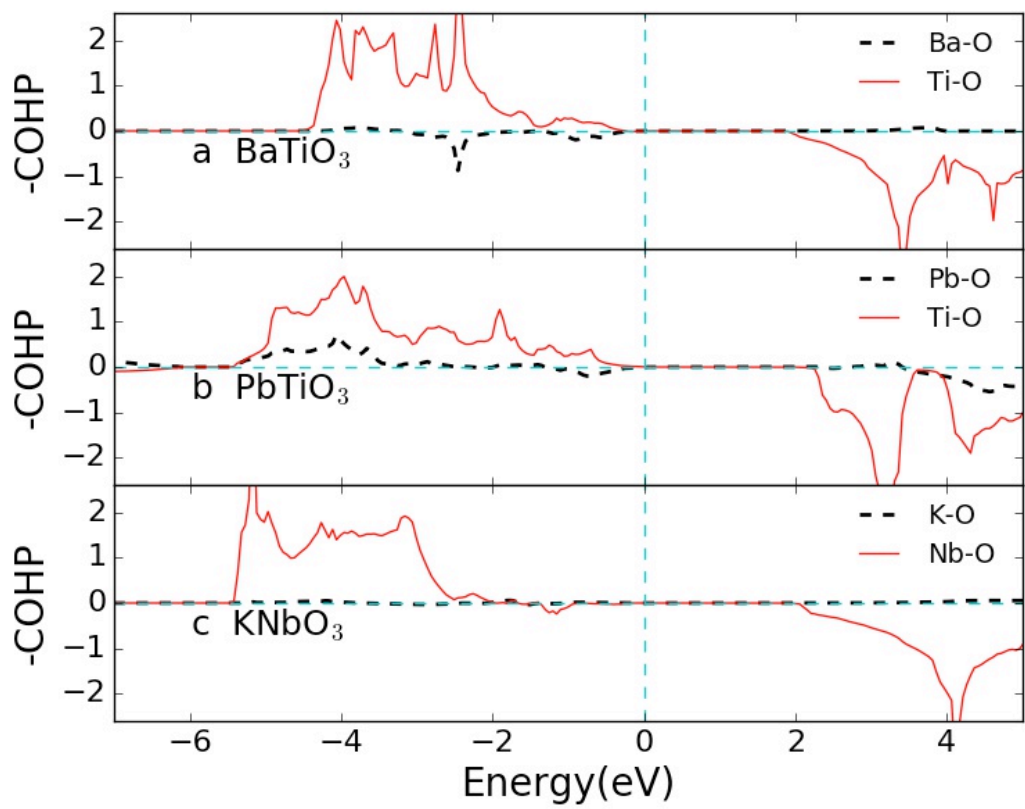
Supplementary Figure 2: Phase transitions in BiFeO₃ induced by hydrostatic-pressure (P) and doping (ρ_{free}). Panels (a) and (c) show the enthalpy (or energy) of different polymorphs for BiFeO₃ as a function of hydrostatic-pressure and doping, respectively. Panels (b) and (d) show the variation of volume as a function of hydrostatic-pressure and doping, respectively.



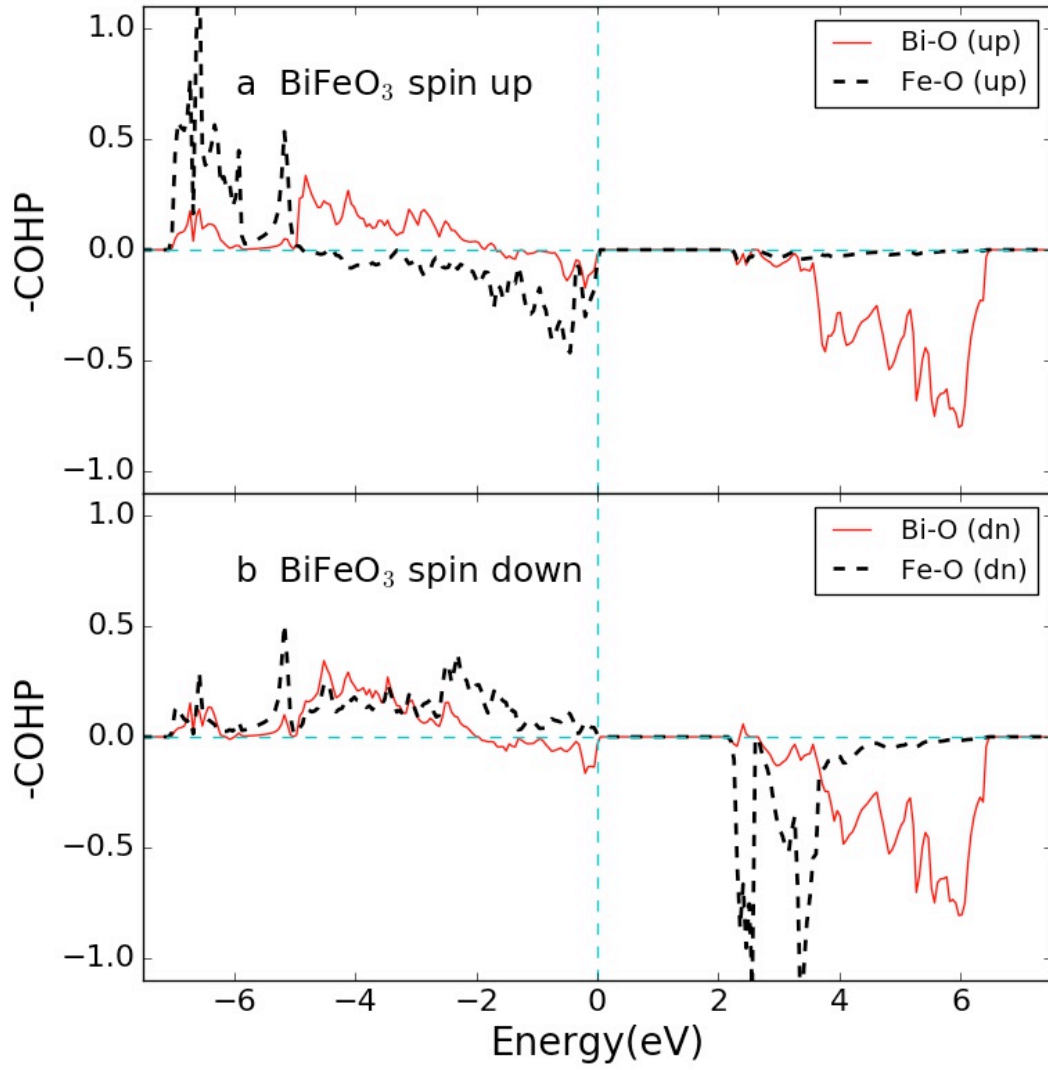
Supplementary Figure 3: Obtained crystal structures of BiFeO_3 under negative pressure (-4 GPa) and n -doping (0.25 |e|/f.u.). Panels (a)~(c) show different views of the Pc phase obtained under negative pressure, which is qualitatively identical to the one obtained under the n -doping.



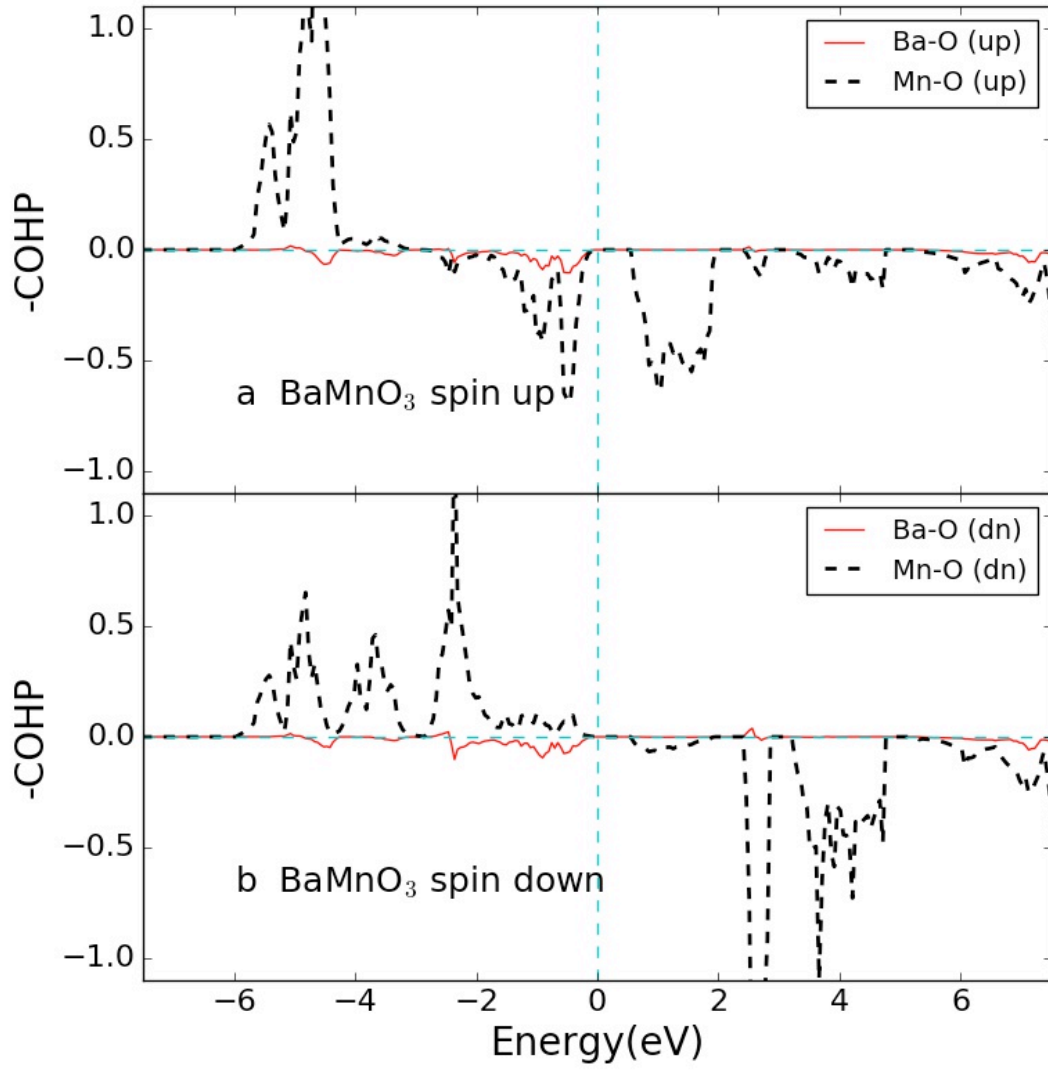
Supplementary Figure 4: Phase transitions in LaAlO₃ induced by hydrostatic-pressure (P) and doping (ρ_{free}). Panels (a) and (b) show the enthalpy (or energy) of cubic ($Pm-3m$) and rhombohedral ($R-3c$) phases for LaAlO₃ as a function of hydrostatic-pressure and doping, respectively.



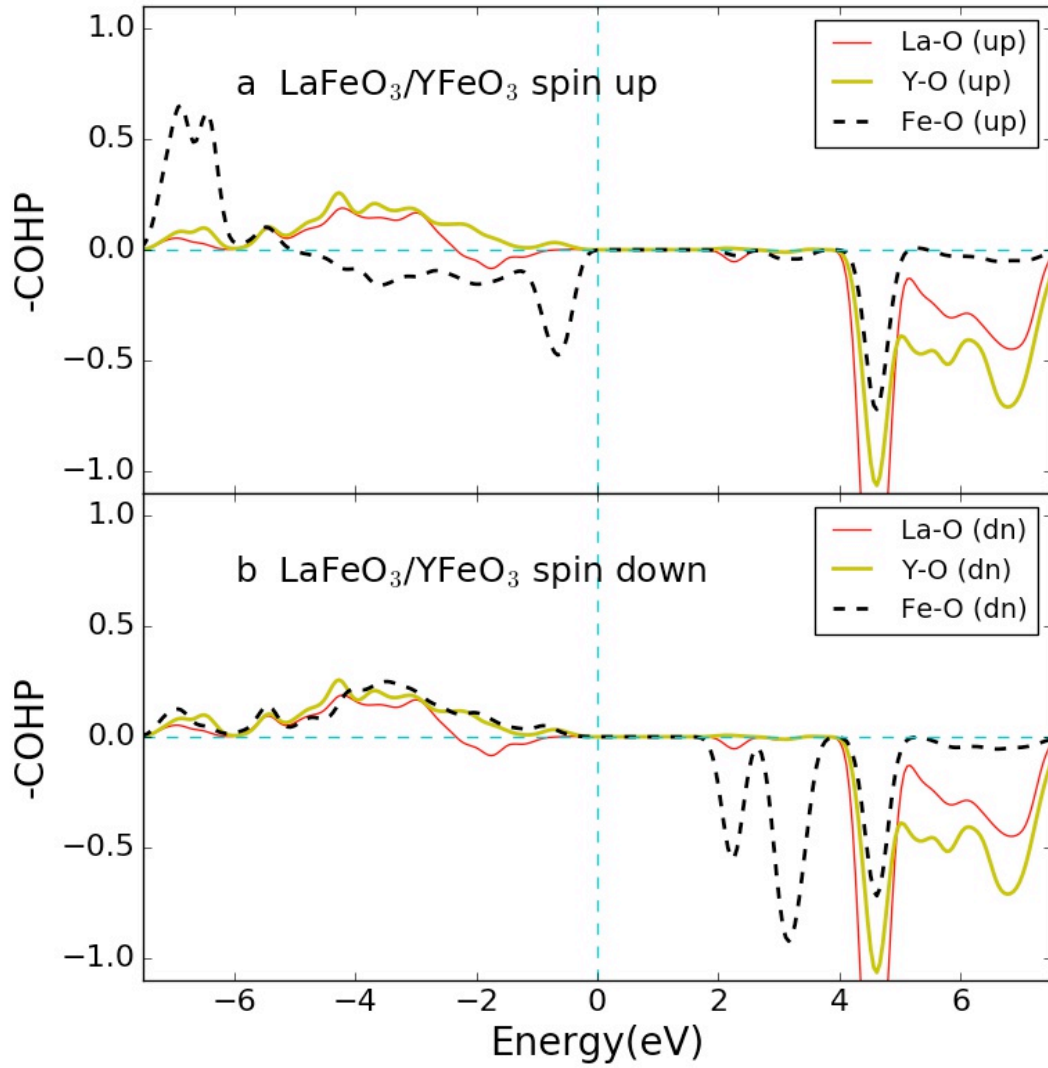
Supplementary Figure 5: COHP (Crystal Orbital Hamilton Population) curves obtained for ferroelectric $P4mm$ BaTiO₃ (a), PbTiO₃ (b), and KNbO₃ (c).



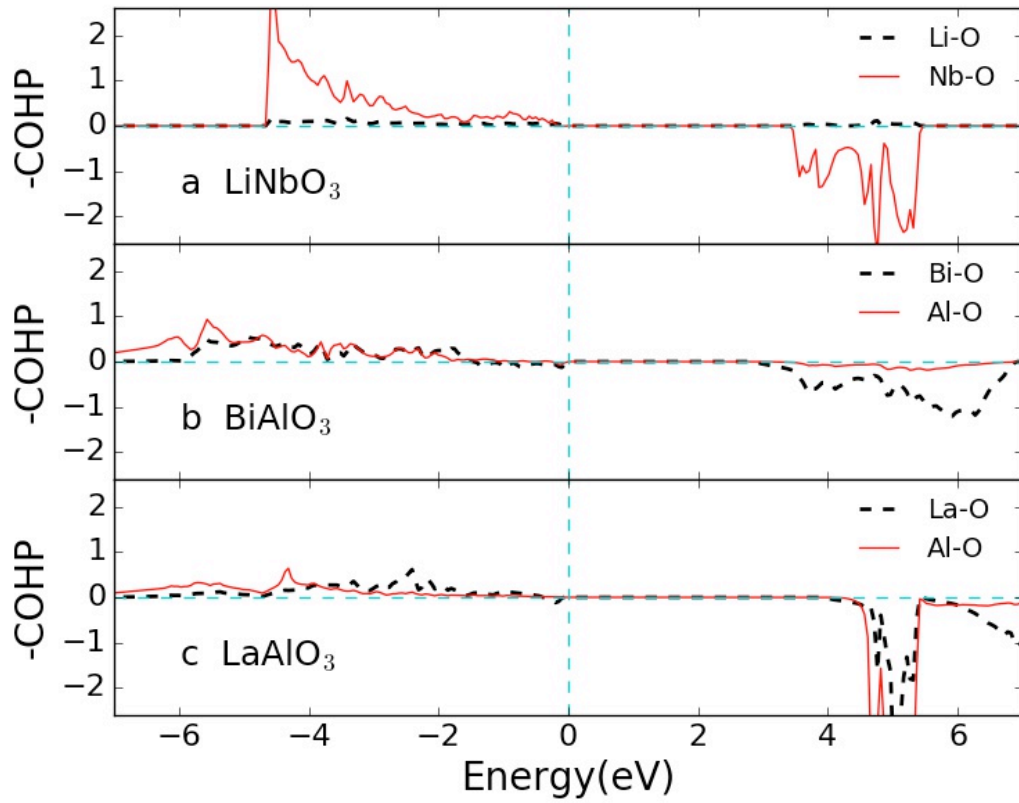
Supplementary Figure 6: COHP curves obtained for ferroelectric *R3c* BiFeO₃; we show spin-up (a) and spin-down (b) contributions separately.



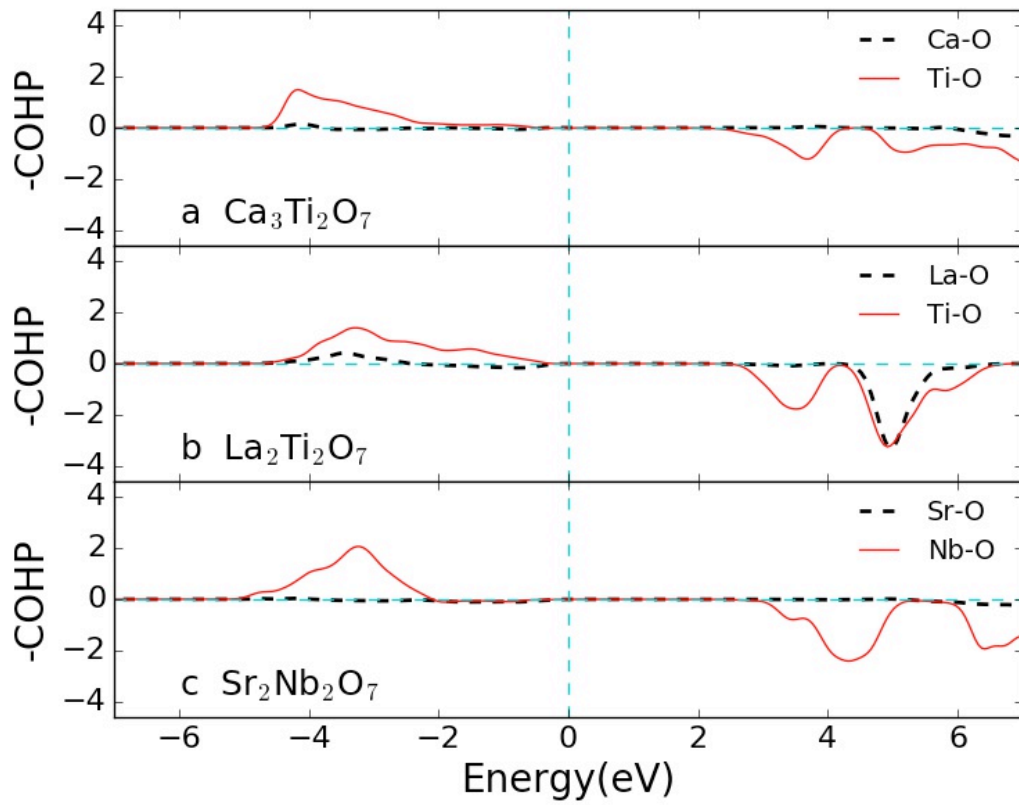
Supplementary Figure 7: COHP cuves obtained for ferroelectric $R3m$ BaMnO₃, showing the spin-up (a) and spin-down (b) contributions.



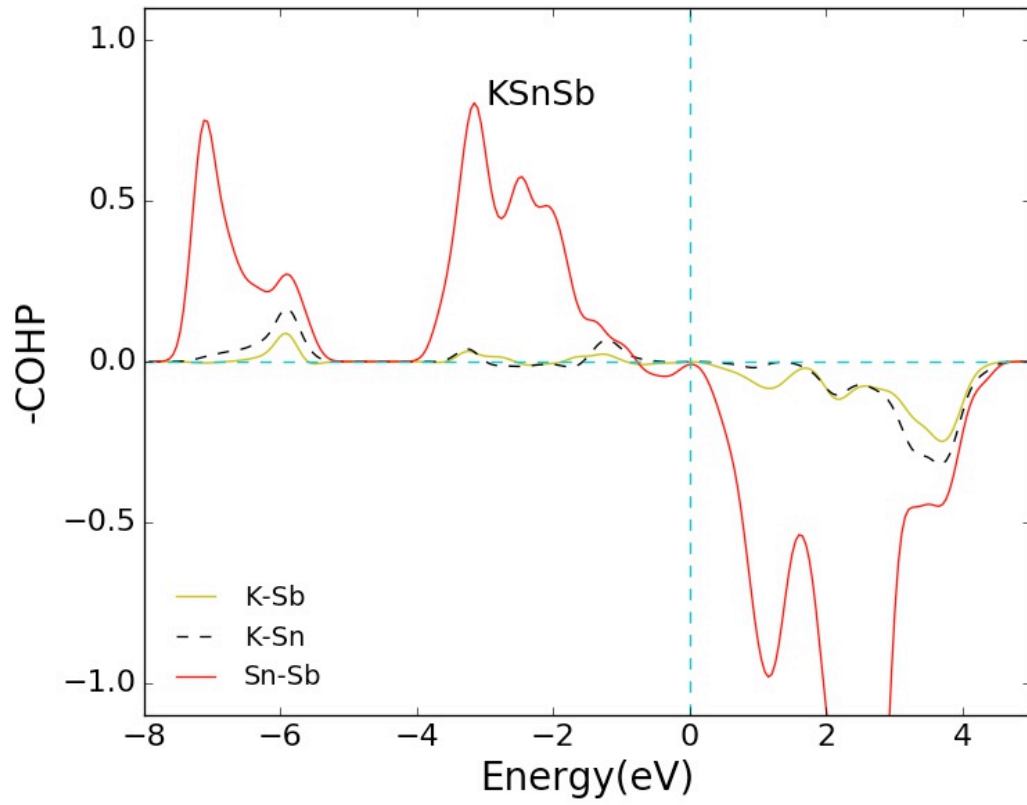
Supplementary Figure 8: COHP curves obtained for (001)-oriented $Pmc2_1$ $\text{LaFeO}_3/\text{YFeO}_3$ superlattice, showing the spin-up (a) and spin-down (b) contributions.



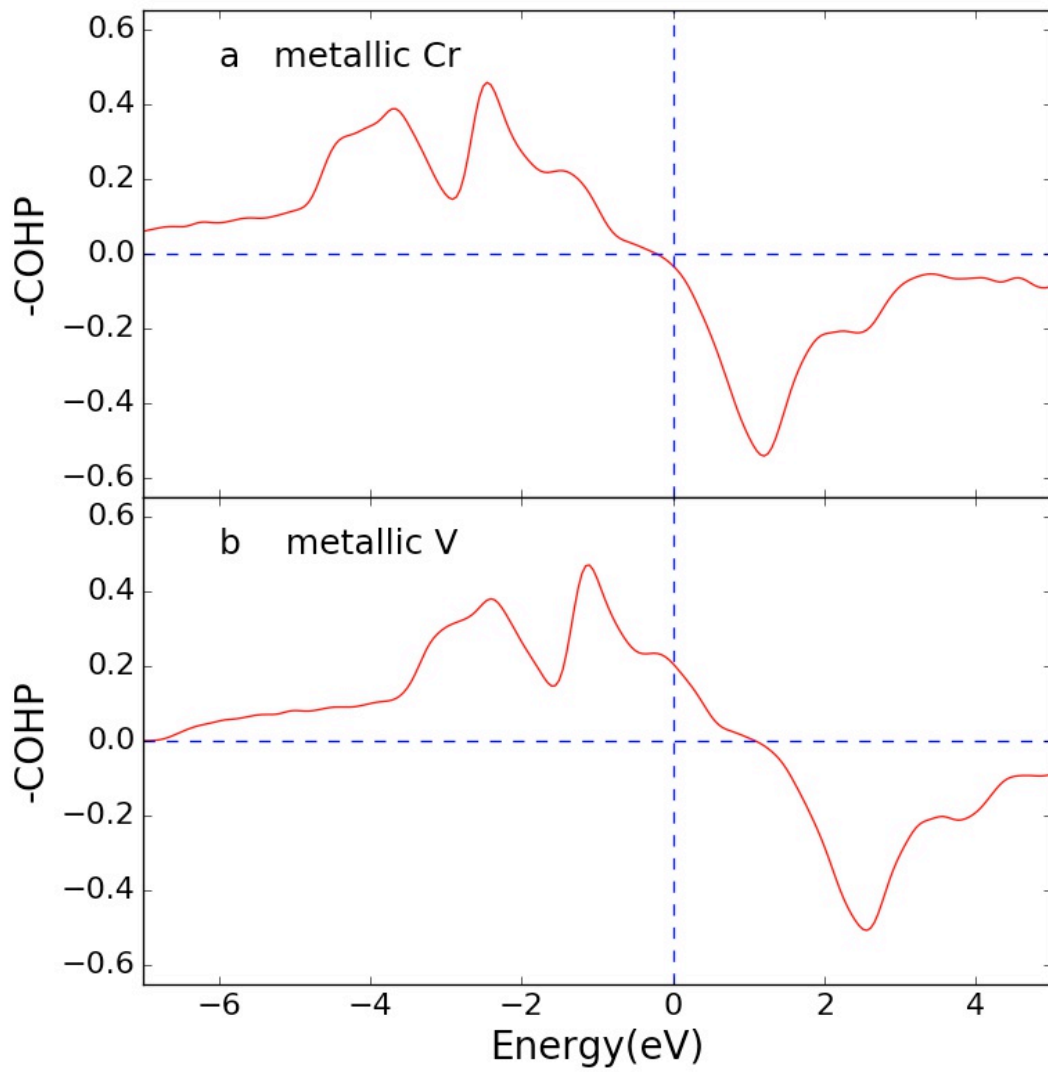
Supplementary Figure 9: COHP curves obtained for ferroelectric $R3c$ LiNbO_3 (a), $R3c$ BiAlO_3 (b), and $R-3c$ LaAlO_3 (c).



Supplementary Figure 10: COHP curves obtained for layer perovskites $\text{Ca}_3\text{Ti}_2\text{O}_7$ (a), $\text{La}_2\text{Ti}_2\text{O}_7$ (b), and $\text{Sr}_2\text{Nb}_2\text{O}_7$ (c).



Supplementary Figure 11: COHP curves obtained for KSnSb.



Supplementary Figure 12: COHP curves obtained for Cr (a) and V (b).

Supplementary Table 1: Electronic dielectric constant, Born effective charges, and lowest TO and LO modes, for the bulk perovskites in cubic paraelectric structures. The LO-TO splitting is reported as well (last column).

structure	ϵ_∞	Z_A	Z_B	Z_{O1}	Z_{O2}	$\omega_{TO}(\text{cm}^{-1})$	$\omega_{LO}(\text{cm}^{-1})$	$\Delta\omega(\text{cm}^{-1})$
BaTiO ₃	7.12	2.73	7.73	-6.15	-2.15	-138	172	310
PbTiO ₃	8.86	3.87	7.53	-6.26	-2.57	-119	98	217
BiFeO ₃	11.07	6.36	3.86	-3.40	-3.41	-210	134	344
BiAlO ₃	8.13	6.29	2.82	-2.38	-3.36	-165	227	392
KNbO ₃	6.52	1.14	9.66	-7.32	-1.74	-187	178	365
LiNbO ₃	6.23	1.24	9.47	-7.30	-1.70	-240	-141	99

Supplementary Note 1: The quasi-homogeneous field

By displacing a plane of Ti atoms (located at $z \approx 2.0 \text{ \AA}$, see Fig. 4 in the main text) along z direction, we create an xy dipole plane, which generates effective electric field along z direction in the supercell. Such electric field (along z direction) can be calculated by

$$E_{k,z} = \frac{F_{k,z}}{Z_k^*} \quad (1)$$

Here, $E_{k,z}$ is the effective electric field acting on the k -th atom; $F_{k,z}$ is the force acting on the k -th atom resulted from the xy dipole plane; and Z_k^* is the dynamical charge of k -th atom. Alternatively, the electric field can also be derived from

$$E_z = \frac{1}{|e|} \frac{d[\Delta V(z)]}{dz} \quad (2)$$

Here, $\Delta V(z)$ is the potential energy difference between $V_{\text{dist}}(z)$ and $V_{\text{cubic}}(z)$ (see Fig. 6 in the main text); $|e|$ is the absolute value of electron's charge.

In Supplementary Figure 1, the xy plane of dipoles lead to a quasi-homogeneous electric field of $\sim 0.0077 \text{ V/\AA}$, in the intermediate region of the supercell ($z < -8.0 \text{ \AA}$ or $z > 12 \text{ \AA}$). According to the Supplementary Eq. (2), such electric field in the intermediate region, as derived from the potential, is $\sim 0.0076 \text{ V/\AA}$.

Supplementary Note 2: Volume effects of doping, and induced transitions

In order to understand the similarity between doping and pressure in inducing phase transitions, we consider two typical perovskites (i.e. BiFeO_3 and LaAlO_3). BiFeO_3 and LaAlO_3 present rhombohedral crystal structures at their ground state, with $R3c$ and $R-3c$ symmetries, respectively. In order to understand the phase transitions in BiFeO_3 and LaAlO_3 , we use the FINDSYM¹ code (typically with a tolerance of 0.01) to analyze the symmetries of various phases.

On one hand, as shown in panels (a) and (b) of Supplementary Figure 2, hydrostatic compression induces a transition from rhombohedral $R3c$ to orthorhombic $Pbnm$ at $\sim 2\text{GPa}$ for BiFeO_3 . In addition, at negative pressure of $\sim -3.5\text{GPa}$, the transition from rhombohedral $R3c$ to a monoclinic Pc phase occurs in BiFeO_3 . This Pc phase is shown in Supplementary Figure 3: It is not a perovskite structure and, as far as we can tell, had not been reported earlier; we obtained it after a long relaxation to reach our demanding threshold for the maximum forces. Note that we also considered a phase Cc that never gets to be the ground state under pressure; this is the super-tetragonal structure amply discussed for BFO in the literature.

Interestingly, as shown in Supplementary Figure 2, charge doping induces the same transition sequence in BiFeO_3 . More precisely, p-doping causes a phase transition from $R3c$ to $Pbnm$; while the n-doping induces a phase transition from $R3c$ to Pc .

We also checked the phase transitions in LaAlO_3 induced by both pressure and doping. Note that the experiment shows that LaAlO_3 undergoes pressure-induced transformation from rhombohedral $R-3c$ to cubic $Pm-3m$ at $\sim 14\text{GPa}$ (Ref. 2). In Supplementary Figure 4, our first-principles results reproduce this same transition, albeit at a higher pressure of about 32 GPa. Similarly, p-doping causes the same rhombohedral-to-cubic transformation.

Supplementary Note 3: COHP analysis

Here we discuss whether the volume changes upon doping can be traced back to the features of the electronic states that are filled or emptied. Let us note that all our considered oxides belong to one of these two groups: (i) perovskites where the transition metal based levels are empty (d^0), or (ii) perovskites with partially filled transition metal based levels (d^n , with $n > 0$). In the second case, both the lowest empty and highest filled levels are anti-bonding. Hence one may speculate that n/p -doping will populate/deplete anti-bonding states so that they will cause a volume expansion/contraction in agreement with our results. In contrast, this purely first-order reasoning is not fully appropriate for the first group of compounds (d^0). Here, n -doping will populate anti-bonding orbitals thus leading to a volume expansion in agreement with the calculations; on the other hand, p -doping will depopulate slightly bonding orbitals, and thus should also lead to some volume expansion, in disagreement with our simulation results. Nevertheless, a slightly refined argument for the p -doping of d^0 compounds seems in order: Note that the depleted levels have a strong oxygen character and, thus, because of the polarity of the system, p -doping should lead to strong second-order effects, i.e., orbital mixings tending to counteract the loss of bonding electrons around the more electronegative oxygen centers. In other words, the volume will tend to contract, as found in our calculations, so as to restore as much as possible the chemical bonding lost because of the p -doping. Such second-order effects, which may be quite strong in the d^0 compounds, should not be relevant for the d^n ones where p -doping depopulates orbitals with larger weight in the (less-electronegative) cations.

In order to check these ideas, we run the COHP (Crystal Orbital Hamilton Populations) analysis using the lobster code³⁻⁷. Generally, for perovskite or layered-perovskite materials with the chemical formula ABO_3 , $A_2B_2O_7$ and $A_3B_2O_7$, we do the COHP analysis for the A-O and B-O interactions. For the rest materials, we do the analysis for La-O, Y-O and Fe-O for $LaFeO_3/YFeO_3$, K-Sb, K-Sn, Sn-Sb for

KSnSb, Cr-Cr for Cr metal and V-V for V metal, respectively. For all the interactions considered in our COHP analysis, only first nearest-neighbouring atom pairs are considered. For example, in LaFeO₃/YFeO₃ superlattice, in LaO₈ polyhedron, the La-O pair with the shortest bond length is selected as the representative case of the COHP La-O interaction.

In general, the picture introduced above is mostly substantiated by the COHP analysis of perovskite or layered-perovskite materials. KNbO₃ is the only compound among those we have studied that does not seem to follow the bonding pattern of the d⁰ compounds. However, we note that the same type of ideas do not provide an appropriate explanation for other material types. For instance, both V and Cr metals are predicted to contract/expand under p/n doping according to the results of Fig. 9a. The metal V exhibits bonding states both below and above the Fermi level (Supplementary Figure 12b) so that *p*-doping and *n*-doping should lead to volume expansion and contraction, respectively. This is in contradiction with the actual DFT results of Fig. 9c. The metal Cr exhibits bonding/anti-bonding states below/above the Fermi level (Supplementary Figure 12a) so that both *p*-doping and *n*-doping should lead to volume expansion. This is in contradiction with the actual DFT results of Fig. 9c for the case of *p*-doping. Further, second-order effects are not expected to be important for these systems.

Hence, in our opinion there is no clear evidence supporting the above outlined bonding picture as being the main factor behind the results of Figure 9a. Rather, we tend to favor the interpretation that the obtained volume effects may be the consequence of a simple and crude *steric* mechanism of – namely, that electrons do occupy space – which prevails over the bonding characteristics of the (de)populated states.

Supplementary Note 4: Phonon frequencies and LO-TO splitting calculations

In order to search for possible hyperferroelectric materials, we performed phonon frequency and LO-TO splitting calculations for all the cubic and layered perovskites studied in the article. As ferroelectrics, they must be characterized by at least one unstable phonon mode in the centrosymmetric paraelectric structure. If we restrict ourselves to proper ferroelectrics, this mode should be an infrared-active TO mode at the Γ -point (differently from improper ferroelectrics, whose polarization is driven by higher-order coupling of polar distortions with unstable non-polar modes). Usually in these systems, only the TO mode is unstable, while the corresponding LO mode is much higher in energy, and generates a strong macroscopic electric field which favors a suppression of polarization, unless properly screened by metallic contacts or domain formation. However, it was put in evidence in Supplementary Ref. [8] that having large LO-TO splitting is by no means a requirement of all ferroelectrics, and in fact systems having both unstable TO and LO modes could be envisaged. These systems, termed hyperferroelectrics in Supplementary Ref. [8], have the remarkable quality to be able to sustain the macroscopic polarization *in open-circuit boundary conditions* even in their pristine, single-phase insulating state, with no need of screening. In other words, for hyperferroelectrics, the depolarization field is small enough to be counterbalanced by the zero-field energy gain associated to the polar distortion.

The amplitude of LO-TO splitting at the Γ -point is a non-analytic contribution to the dynamical matrix, given by:

$$D_{ij}^{\alpha\beta} = \lim_{q \rightarrow 0} \frac{4\pi e^2}{\Omega} \frac{\left(\sum_{\gamma} Z_i^{\gamma\alpha} q_{\gamma} \right) \left(\sum_{\delta} Z_j^{\delta\beta} q_{\delta} \right)}{\sum_{\gamma\delta} Z_i^{\gamma\alpha} q_{\gamma} \epsilon_{\gamma\delta}^{\infty} q_{\delta}} \quad (3)$$

where i, j are atomic indices, $\alpha, \beta, \gamma, \delta$ are Cartesian indices, $\epsilon_{\gamma\delta}^{\infty}$ is the electronic dielectric tensor, $Z_i^{\alpha\gamma}$ is the Born effective charge tensor of the i^{th} atom, Ω is the cell volume, and e is the electron charge. Thus, a small LO-TO splitting requires large

electronic dielectric tensor and/or small effective charges.

For our calculations, we employ VASP to obtain all the necessary ingredients: Born effective charges and the dielectric tensor entering Supplementary Eq.(3), plus the analytic part of the dynamical matrix, added to the non-analytic term. The total matrix is then diagonalized to obtain the phonon frequencies of the system at the Γ -point.

In Supplementary Table 1, we report the calculated dielectric constants and effective charges for perovskites in their cubic, high-temperature paraelectric structure. Due to cubic symmetry, the dielectric tensor reduces to just one value, and the effective charge tensors are all diagonal, with only four independent values, i.e. the A-site atom charge, the B-site atom charge, a single-degenerate oxygen charge in the B-O ligand direction (O1), and a double-degenerate oxygen charge in the B-O transverse direction (O2), which mainly involves A-O coupling.

According to the effective charges, the six examined compounds can be separated in two different classes: titanates and niobates, characterized by strong anomalies along the B-O1 ligand bonds, and the bismuth perovskites, for which the largest anomaly is driven by Bi-O2 hybridization. In Supplementary Table S1, we report for each system the calculated energy-lowest IR-active phonon frequencies of the double-degenerate TO mode (which is soft for all the systems) and the single-degenerate LO mode. For all systems except BiFeO₃, this mode is also the energy-lowest overall, thus it corresponds to the soft mode leading to the ferroelectric ground-state displacement. For BiFeO₃, there are other two, more stable, triple-degenerate non-polar modes (associated to concerted rotations of the O₆ octahedra) which of course do not display any splitting and are not considered here.

We see that only LiNbO₃ displays the sought for properties of having a soft LO mode; this is owed to a LO-TO splitting which is about a factor-three smaller than all the other compounds. This is especially surprising in comparison to KNbO₃ since, as we see from Supplementary Table 1, the 'ingredients' contributing to the non-analytical term are quite similar for the two of them.

In order to gain some physical hints about the reason which makes LiNbO₃ so

special, we analyzed by inspection the atomic displacements associated to the Γ -point LO modes under examinations. Surprisingly, we found that LiNbO_3 is the only system for which the oxygens of the cell do not move in phase; specifically, the soft LO mode is characterized by large Li displacements in phase with the smaller displacements of its co-planar oxygen, while Nb with its two coplanar oxygens move in the opposite direction. For all the other perovskites, A-site and B-site cations always move oppositely, while the three oxygens move sometimes in phase with the A-site, sometimes with the B-site, but always in phase among themselves. Notice that this peculiarity is not displayed by the TO mode, in which the oxygens move in phase even for LiNbO_3 . Note that the hyperferroelectric character of LiNbO_3 and related compounds has been discussed in Supplementary Ref. 9.

We also tested possible quantitative parameters as soft LO detector; a typical candidate is the mode effective charge, which in the simplest cases is somewhat related to the LO-TO splitting, as described by the Lyddane-Sachs-Teller expression. Unfortunately, however, the simple magnitude of the mode effective charge (eventually squared and scaled by the dielectric constant) turns out to not be a valid indicator. This suggests that the LO mode is tightly coupled with other displacements, thus the energy gain associated to the mode cannot be simply derived by the displacement of that single mode alone.

Now let us move to analyze three layered perovskites, which are all found to be hyperferroelectrics.

a) $\text{Ca}_3\text{Ti}_2\text{O}_7$ (CTO327): In the high-symmetry $I4/mmm$ tetragonal structure, the analytic dynamical matrix is characterized by a double-degenerate, soft, in-plane mode which, upon introduction of the non-analytic part, split into $\omega_{TO} = -91.1 \text{ cm}^{-1}$ and $\omega_{LO} = -29.4 \text{ cm}^{-1}$. The same splitting is found along the symmetry-equivalent $q=[1,0,0]$ and $[0,1,0]$ directions, while for $q=[0,0,1]$ the lowest frequency remains double degenerate, thus there is no polar instability in the orthogonal direction. The dielectric constant values ($\epsilon_{xx}^\infty = 5.77$, $\epsilon_{zz}^\infty = 5.64$) are typical of wide band-gap oxides.

Regarding Born effective charges, we obtain $Z_{Ca}=2.59$ and 2.28 in-plane, 2.27 and 3.0 out-of-plane; $Z_{Ti}=7.29$ in-plane and 6.29 out-of-plane; for planar oxygens, $Z_{O}= -5.82$ and -2.05 in-plane, and -1.71 out-of-plane; finally, for apical oxygens, $Z_{O}= -1.97$ and -2.06 in-plane, and -4.46 and -5.1 out-of-plane.

b) $\text{La}_2\text{Ti}_2\text{O}_7$ (LTO227): The analytic matrix calculated for the high-symmetry $Cmcm$ phase presents as much as five, unstable singlet modes, with the overall lowest at $\omega = -127.13 \text{ cm}^{-1}$. After the inclusion of the non-analytical part, nothing changes along the $q=[1,0,0]$ direction (parallel to the Ti-O bonds) or along the $[0,1,0]$ direction (that is the stacking direction). Thus, in these directions the five modes are either TO or unpolar LO modes. On the other hand, for $q=[0,0,1]$ (which is the spontaneous polarization direction, in fact, see Suppl. Ref. [10]) two out of the five modes are shifted above in energy, so they must be polar LO modes. Of these two, only one is unstable, but remarkably it is also the lowest overall. Its calculated energy is $\omega_{LO} = -126.65 \text{ cm}^{-1}$, thus the split with respect to the purely analytic value is as small as 0.48 cm^{-1} . The nature of this polar instability, related to the uncompensated antiferrodistortive distortion of the perovskite, is discussed in full detail in Suppl. Ref. [10], together with Born effective charges.

c) $\text{Sr}_2\text{Nb}_2\text{O}_7$ (SNO227): this material, which is isostructural to $Cmcm$ LTO227, displays two single-degenerate unstable modes at -50.8 cm^{-1} and -34.3 cm^{-1} before LO-TO splitting. The inclusion of splitting leaves these modes unchanged along $q=[1,0,0]$ and $[0,1,0]$ directions, while along $q=[0,0,1]$ the lowest in energy shifts to a value $\omega_{LO} = -37.1 \text{ cm}^{-1}$, corresponding to a split as small as 13.7 cm^{-1} .

Supplementary References

1. Stokes, H. T. & Hatch, D. M. Findsymb: program for identifying the space-group symmetry of a crystal. *J. Appl. Crystallogr.* 38, 237–238 (2005).
2. Bouvier, P. & Kreisel, J. Pressure-induced phase transition in LaAlO_3 . *J. Phys.: Condens. Matter* 14, 3981–3991 (2002).
3. Dronskowski, R. & Blöchl P. E. Crystal orbital Hamilton populations (COHP): energy-resolved visualization of chemical bonding in solids based on density-functional calculations. *J. Phys. Chem.* 97, 8617–8624 (1993).
4. Deringer, V. L., Tchougreeff, A. L., & Dronskowski, R. Crystal Orbital Hamilton Population (COHP) Analysis As Projected from Plane-Wave Basis Sets. *J. Phys. Chem. A* 115, 5461–5466 (2011).
5. Maintz, S., Deringer, V. L., Tchougreeff, A. L. & Dronskowski, R. *J. Comput. Chem.* 34, 2557–2567 (2013).
6. Maintz, S., Deringer, V. L., Tchougréeff, A. L., Dronskowski, R. LOBSTER: A tool to extract chemical bonding from plane-wave based DFT. *J. Comput. Chem.* 37, 1030–1035 (2016).
7. Maintz, S., Esser, M. & Dronskowski, R. Efficient Rotation of Local Basis Functions Using Real Spherical Harmonics. *Acta Phys. Pol. B* 47, 1165–1175 (2016).
8. Garrity, K. F., Rabe, K. M. & Vanderbilt, D. Hyperferroelectrics: Proper Ferroelectrics with Persistent Polarization. *Phys. Rev. Lett.* 112, 127601 (2014).
9. Li, P., Ren, X., Guo, G.-C. & He, L. The origin of hyperferroelectricity in LiBO_3 ($\text{B} = \text{V}, \text{Nb}, \text{Ta}, \text{Os}$). *Scientific Reports* 6, 34085 (2016).
10. López-Pérez, J. & Íñiguez, J. Ab initio study of proper topological ferroelectricity in layered perovskite $\text{La}_2\text{Ti}_2\text{O}_7$. *Phys. Rev. B* 84, 075121 (2011).